Tribology International 81 (2015) 112–128

Contents lists available at ScienceDirect

Tribology International

journal homepage: www.elsevier.com/locate/triboint

Multi-scale friction modeling for sheet metal forming: The boundary lubrication regime

J. Hol [a,*], V.T. Meinders [b], M.B. de Rooij [b], A.H. van den Boogaard [b]

[a] Innprove Solutions, P.O. box 217, 7500 AE Enschede, The Netherlands
[b] University of Twente, Faculty of Engineering Technology, chair of Nonlinear Solid Mechanics, P.O. box 217, 7500 AE Enschede, The Netherlands

ARTICLE INFO

Article history:
Received 6 April 2014
Received in revised form
20 July 2014
Accepted 22 July 2014
Available online 1 August 2014

Keywords:
Boundary lubrication
Ploughing
Multi-scale friction modeling
Sheet metal forming

ABSTRACT

A physical based friction model is presented to describe friction in full-scale forming simulations. The advanced friction model accounts for the change in surface topography and the evolution of friction in the boundary lubrication regime. The implementation of the friction model in FE software codes is discussed. Results show that friction coefficients vary in space and time, and depend on local process conditions such as the nominal contact pressure and the plastic strain in the sheet material. The advanced friction model is validated by two small-scale forming processes, proving the enhanced predictive capabilities of FE simulations. The moderate increase in FE computation time, compared to using a Coulomb based friction model, demonstrates the efficiency of the proposed friction model.

1. Introduction

Significant improvements have been made in the numerical simulation of metal forming processes in the last decade. An accurate forming analysis can however only be made if, amongst others, the friction conditions between the sheet material and the tools are described accurately. In the majority of FE simulations a simple Coulomb friction model is used. The Coulomb friction model does not include the influence of important parameters such as pressure, punch speed or the type of lubricant used. Hence, a physical-based friction model which accounts for a varying friction coefficient will enhance the accuracy of numerical forming simulations [1–4].

Boundary lubrication is a common lubrication regime in sheet metal forming. In this regime, a normal contact load is solely carried by contacting surface asperities. The real area of contact, playing an important role in characterizing friction, relies on the roughness characteristics of both the tool and the workpiece surface. The workpiece surface is liable to changes due to flattening and roughening mechanisms, changing the real contact area.

The main flattening mechanisms during sheet metal forming, which tend to increase the real area of contact, are flattening due to normal loading, flattening due to sliding and flattening due to combined normal loading and deformation of the underlying bulk material. Roughening of asperities, observed during deformation of the bulk material without applying a normal load to the surface, tends to decrease the real area of contact [5,6]. Most of the theoretical models describing the flattening behavior of asperities continue the pioneering work of Greenwood and Williamson [7], who proposed an elastic contact model that accounts for a stochastic description of rough surfaces. Over recent years, modifications have been made to this model to account for arbitrarily shaped asperities [8], plastically deforming asperities [9,10], the interaction between asperities [8,11] and the influence of stretching the underlying bulk material [12,13]. Another technique to describe the flattening behavior of asperities relies on variational principles, first introduced by Tian and Bhushan [14]. Variational principles account for the fractal behavior of rough surfaces and include the long-range elastic coupling between contacting asperities. Elastic perfectly plastic contact conditions, including the unloading behavior of asperities, can be described using this approach. Besides the analytically based models described above, techniques can be used that account for a deterministic description of rough surfaces. In conjunction with, for example, FE techniques, realistic 3D surfaces can be examined under different loading and bulk straining conditions. Korzekwa et al. [15] were one of the first who adopted a plane strain FE approach to derive empirical relations for the description of asperity flattening under combined normal loading and straining of the bulk material. Although the FE approach has proven its applicability in many engineering applications, simplifying assumptions have to be made to ensure reasonable computation times with respect to modeling 3D rough surface textures.

Compared to normal loading only, a further increase in real contact area can be caused by sliding. The increase in real contact area reduces the mean pressure at contact spots, accommodating the additional shear stresses. The increase in real contact area is

* Corresponding author. Tel.: +31 534894567; fax: +31 534893471.
E-mail address: j.hol@innprove.com (J. Hol).

http://dx.doi.org/10.1016/j.triboint.2014.07.015
0301-679X/

referred to as junction growth [16], and is a known phenomenon for dry contacts [17–20]. In this case, the required shear stress to initiate junction growth is introduced by the adhesion effect between dissimilar materials. For lubricated contacts, a similar effect such as junction growth has been observed by Emmens [21] and Lo and Tsai [22].

Friction is caused by ploughing and adhesion between contacting surface asperities. Wilson [23] and Challen and Oxley [24,25] developed models to account for these effects. Wilson [23] treated the effect of adhesion and ploughing on friction separately, while Challen and Oxley took the combined effect of ploughing and adhesion into account. Challen and Oxley deduced slip-line fields to describe friction between one wedge-shaped asperity and a flat soft workpiece surface. Friction between multiple tool asperities and a flat soft counter surface can be obtained by describing the tool surface in terms of stochastic parameters [8]. To establish the translation from single asperity scale to multiple asperity scale, the summit height distribution of the tool, the asperity density and the mean radius of tool asperities are required. However, such ploughing models tend to lose their applicability under high fractional real contact areas. In these areas, tool asperities form contact patches which penetrate into the softer workpiece material [26,27]. The frictional behavior of the contacting surfaces now depends on the geometry of the contact patches, rather than the geometry of the individual asperities. In addition, the required stochastic parameters are known to be dependent on the resolution of the measured surface texture [28]. Ma et al. [29] proposed a multi-scale friction model that accounts for asperities forming contact patches under high fractional real contact areas. A deterministic surface description is used in their approach, which excludes the use of a summit height distribution, the asperity density and the mean asperity radius, and therefore excludes possible scale dependency problems.

A boundary lubrication friction model is presented in this paper. A friction framework has been developed that comprises existing, adapted and newly developed models. Because micro-mechanical friction models are generally regarded as too cumbersome to be used in large-scale FE simulations, the choice of the implemented models is a trade-off between accuracy and computational efficiency. This will yield a physically based friction model that is still computationally attractive for use in large-scale forming simulations. The framework distinguishes 3 stages. In the first stage, the input step, surface characteristics and material properties are defined. A method to measure 3D surfaces and an experimental procedure to obtain model parameters is discussed. Stage 2, the asperity deformation step, includes models to describe surface changes due to normal loading, deformation of the underlying bulk material and sliding, see Section 2. The models are based on a stochastic description of a rough workpiece surface in contact with a flat tool surface, and provide an expression for the fractional real area of contact. A non-linear work-hardening normal loading model is presented which is based on energy and volume conservation laws. Asperity flattening due to combined normal loading and deformation of the underlying bulk material has been described by the flattening model proposed by Westeneng [8]. The increase in real contact area due to sliding is captured by adopting the junction growth theory as proposed by Tabor [16]. The final stage, the friction evaluation step, accounts for the influence of ploughing and adhesion on friction. The contact model of Ma et al. [29], which was originally developed to describe friction in extrusion processes, has been adapted to model friction in metal forming processes, see Section 3. In contrast to the asperity deformation models, this model accounts for a deterministic description of the rough workpiece and tool surface, in which the calculated deformation of workpiece asperities in stage 2 is used to adapt the surface texture of the workpiece. The plateaus of the flattened workpiece asperities are assumed to be perfectly flat, in which the harder tool asperities are penetrating. The summation of shear forces acting on individual contact patches (collection of penetrating tool asperities) is used to finally obtain the friction coefficient. The final section describes the implementation of the boundary lubrication friction model in an FE software code. Two deep drawing applications will be discussed to demonstrate the applicability of the advanced friction model to large-scale forming simulations.

2. Modeling the deformation behavior of rough surfaces

The models implemented within the asperity deformation step are discussed in this section. First, the normal loading model is discussed in Section 2.1. The influence of sliding on the real contact area is outlined in Section 2.2. Finally, a model for combined normal loading and deformation of the underlying bulk material is discussed in Section 2.3.

2.1. Flattening due to normal loading

In most of the contact models the asperity density, the mean asperity radius and the *summit* height distribution are used to calculate the amount of asperity deformation, which was first introduced by Greenwood and Williamson [7]. Summit based stochastic parameters depend on the resolution of the scanning method used. Westeneng [8] proposed an ideal-plastic contact model that accounts for the *surface* height distribution instead of the *summit* height distribution to describe rough surfaces. The *surface* height distribution is based on measured surface points, which excludes the use of summit based stochastic parameters. The contact model proposed in this section is based on the normal loading model described by Westeneng. The newly developed contact model accounts for work hardening in deforming asperities. Moreover, compared to the contact model of Westeneng, the shear stress between crushing and raising asperities is accounted for.

A rigid and perfectly flat tool is assumed contacting a soft and rough workpiece material. This is considered a valid assumption as the tool surface is in general much harder and smoother than the workpiece surface. The roughness texture of the workpiece is modeled by bars, which can represent arbitrarily shaped asperities, see Fig. 1. The cross sectional area of these bars is taken to be equal to the resolution of the measured (or digitally generated) 3D surface texture. Three stochastic variables are introduced to make the translation from micro-scale to macro-scale modeling of contact: the normalized surface height distribution function of the rough workpiece surface $\phi_w(z)$, the uniform raise of the non-contacting surface U_L (based on volume conservation) and the separation between the tool surface and the mean plane of the rough workpiece surface d_L. The suffix L in d_L and U_L refers to the normal loading step.

The crushing and raising behavior of deformed bars relies on a proper description of the material behavior. In this paper, it is assumed that the maximum pressure a bar can carry equals the hardness H of the material. By approximation, the hardness H is given by

$$H = B\sigma_y \tag{1}$$

with $B \approx 2.8$ for steel materials [16]. The physically based isothermal Bergström van Liempt [30–33] hardening relation is used to describe the yield strength σ_y.

The total plastic strain ε in the bars is related to the reference height λ. The reference height reflects an empirical length scale to be determined from experiments (see Section 4). The reference height is taken to be equal for all bars, see Fig. 1. By using λ,

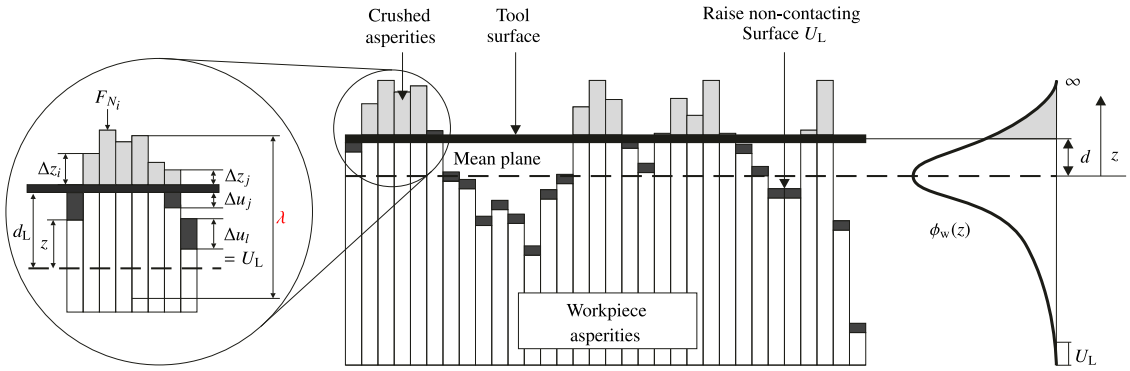

Fig. 1. A rough soft surface crushed by a smooth rigid surface.

a definition for the strain ε can be derived for bars in contact with the tool and bars not in contact with the tool, see Eq. (2) and Fig. 1

$$\varepsilon = \begin{cases} \ln\left(\left|1+\frac{z-d_L}{\lambda}\right|\right) = \ln\left(\left|\frac{\lambda+z-d_L}{\lambda}\right|\right) & \text{for } z+U_L \geq d_L \text{(contact)} \\ \ln\left(\left|1+\frac{U_L}{\lambda}\right|\right) = \ln\left(\left|\frac{\lambda+U_L}{\lambda}\right|\right) & \text{for } z+U_L < d_L \text{(no contact)} \end{cases} \tag{2}$$

2.1.1. Energy conservation

The amount of external energy must equal the internal energy in order to account for energy conservation. The amount of external energy is described by the energy required to crush contacting asperities. The internal energy is described by the energy absorbed by the crushed bars, the energy required to lift up the non-contacting bars and the energy required to shear bars which have a relative motion to each other. The variables used to describe the normal loading model are given in Fig. 1. A distinction is made between bars in contact with the tool, bars which will come into contact due to the raise of asperities and bars which will not come into contact with the tool. The crushing height is described by the variable Δz while the raise of bars is described by the variable Δu. The number of bars in contact with the tool is indicated by N with corresponding crushing heights Δz_i ($i=1,2,\ldots,N$). The number of bars coming into contact with the tool due to a raise of non-contacting asperities is described by N^* with crushing heights Δz_j ($j=1,2,\ldots,N^*$). Hence, the total number of bars in contact with the tool after applying the normal load equals $N+N^*$. The number of bars which will not come into contact during the load step is indicated by N^{**} with corresponding raising heights Δu_l ($l=1,2,\ldots,N^{**}$). The total amount of bars $M=N+N^*+N^{**}$.

The external energy depends on the total number of bars in contact with the tool ($N+N^*$). Normally, the non-contacting bars would raise with a distance Δu_l, but due to the presence of the tool, some of the bars are restricted to raise with a distance of Δu_j only (see bar j in Fig. 1). A certain amount of external energy is required to prevent a raise of $\Delta z_j = \Delta u_l - \Delta u_j$. The energy required to indent contacting bars is given by

$$W_{ext} = \sum_{i=1}^{N} F_{N,i}\Delta z_i + \sum_{j=1}^{N^*} F_{N,j}\Delta z_j = \sum_{k=1}^{N+N^*} F_{N,k}\Delta z_k \tag{3}$$

with $F_{N,k} = H_k \Delta A$ where H_k is obtained by $B\sigma_{y,k}$. ΔA represents the contact area of a single bar. In a later stage, the external and internal energy equations will be written in stochastic form for computational purposes. For this reason, Eq. (3) is rewritten in the following form:

$$W_{ext} = F_N \omega \quad \text{with } \omega = \frac{\sum_{k=1}^{N+N^*} F_{N,k}\Delta z_k}{F_N} \tag{4}$$

In which F_N represents the total force and ω the indentation factor.

The internal energy is the energy absorbed by the crushed bars $W_{int,ab}$ and the energy required to raise the non-contacting bars $W_{int,ri}$. Shear stresses will be present between bars with a relative motion to each other, introducing an additional energy term $W_{int,sh}$ to the equilibrium equation:

$$W_{int} = W_{int,ab} + W_{int,ri} + W_{int,sh} \tag{5}$$

Knowing the definition of the deformation behavior of asperities (Eq. (1)), the absorbed energy $W_{int,ab}$ over $N+N^*$ crushed bars can be written as

$$W_{int,ab} = \sum_{k=1}^{N+N^*} H\Delta z_k \Delta A = B\Delta A \sum_{k=1}^{N+N^*} \sigma_{y,k}\Delta z_k \tag{6}$$

or

$$W_{int,ab} = B\xi \quad \text{with } \xi = \Delta A \sum_{k=1}^{N+N^*} \sigma_{y,k}\Delta z_k \tag{7}$$

Since the contact area of the bars is taken to be equal to the resolution of the scanned (or generated) surface texture, all bars have the same contact area ΔA. The change in $\sigma_{y,k}$ during crushing of asperities should be accounted for as $\int \sigma_{y,k}(\varepsilon)\, d\Delta z_k$ to describe work-hardening effects properly. For computational efficiency, it is assumed that this integral can be approximated by the generalized midpoint rule, hence $\int \sigma_{y,k}(\varepsilon)\, d\Delta z_k = \sigma_{y,k}(\xi\varepsilon)\Delta z_k$. If $\xi = 0$ the initial yield strength is used, if $\xi = 1$ the yield strength at the end of the loading step is used. Since ξ only has an influence on the calculated strain ε, the same result could be obtained by changing the reference height λ (see Eq. (2)). The parameter ξ has therefore been set to one, knowing that the introduced error will be compensated by the calibration procedure of λ. Normal loading experiments will be conducted to obtain a value of λ by reducing the error between experimental and model results. Results of the experiments and the calibration procedure are discussed in Section 4.

$W_{int,ri}$ is described by the sum of energy required to raise N^* bars which comes into contact with the tool after application of the normal load, and to raise N^{**} bars which do not come into contact with the tool:

$$W_{int,ri} = \eta\left(\sum_{j=1}^{N^*} H\Delta u_j \Delta A + \sum_{l=1}^{N^{**}} H\Delta u_l \Delta A\right) = \eta B\Delta A\left(\sum_{j=1}^{N^*} \sigma_{y,j}\Delta u_j + \sum_{l=1}^{N^{**}} \sigma_{y,l}\Delta u_l\right) \tag{8}$$

or

$$W_{\text{int,ri}} = \eta B \beta \quad \text{with } \beta = \Delta A \left(\sum_{j=1}^{N^*} \sigma_{\text{y},j} \Delta u_j + \sum_{l=1}^{N^{**}} \sigma_{\text{y},l} \Delta u_l \right) \tag{9}$$

Eq. (8) includes a persistence parameter η which describes the amount of energy required to lift up the non-contacting bars [8]. A value of $\eta = 0$ means that no energy is required to raise the non-contacting bars, a value of $\eta = 1$ implies that the same amount of energy is required to raise bars as to crush bars.

The shear term $W_{\text{int,sh}}$ describes the shear energy between moving bars. Shear stresses only occur between bars which have a relative motion to each other. These are bars indented by the tool surface, surrounded by non-contacting bars which experience an upward raise due to volume consistency. The additional energy term is described by

$$W_{\text{int,sh}} = \left(1 - \frac{A_{\text{real}}}{A_{\text{nom}}}\right) n_{\text{s}} \sum_{k}^{N+N^*} \tau_{\text{sh},k} A_{\text{sh},k} \Delta s_k \tag{10}$$

with n_{s} representing half of the number of surrounding bars, τ_{sh} the shear strength, A_{sh} the shearing area and Δs the shear distance. n_{s} equals 1 for a plane strain formulation and 2 for a 3D formulation (only bars are accounted for that directly share interfaces). Since the dimensions of the bars are extracted from a scanned (or generated) surface texture, it is assumed that an asperity is described by a cluster of bars. For this reason, 1 bar has most likely not a relative motion with all surrounding bars, as it belongs to a cluster of bars that are crushed together. Therefore, only half of the surrounding bars are accounted for to calculate the number of interfaces that are in relative motion. The shear distance is described by $\Delta s = z - d_{\text{L}} + U_{\text{L}}$, which represents the sum distance between a raising bar (U_{L}) and its neighboring crushing bar ($z - d_{\text{L}}$). It is assumed that the area over which shear occurs can be described by the same distance, that is $A_{\text{sh}} = w \Delta s$ with w being the width of a bar. The shear strength τ_{sh} can be expressed in terms of the yield stress by $\tau_{\text{sh}} = S \sigma_y$ with $S = 1/\sqrt{3}$ following the Von Mises yield criterion. Eq. (10) can now be written as

$$W_{\text{int,sh}} = S \left(1 - \frac{A_{\text{real}}}{A_{\text{nom}}}\right) n_{\text{s}} w \sum_{k}^{N+N^*} \sigma_{\text{y},k} \Delta s_k^2 \tag{11}$$

or

$$W_{\text{int,sh}} = S \psi \quad \text{with } \psi = \left(1 - \frac{A_{\text{real}}}{A_{\text{nom}}}\right) n_{\text{s}} w \sum_{k}^{N+N^*} \sigma_{\text{y},k} \Delta s_k^2 \tag{12}$$

As mentioned before, the energy equations will be rewritten in stochastic form for computational reasons. By doing so, information about neighboring bars is lost, requiring an expression in terms of probabilities to describe the number of interfaces that have a relative motion. The sum over $N+N^*$ bars in Eq. (10) describes the number of bars that are crushed (or will be crushed) rather than the number of interfaces in relative motion. If the real area of contact $A_{\text{real}} = (N+N^*)\Delta A$ is large, the number of interfaces in relative motion will be relatively low. That is, crushing asperities will grow in size and eventually join together to form larger asperities, decreasing the number of bars that have a relative motion with surrounding (raising) bars. For this reason the factor $1 - A_{\text{real}}/A_{\text{nom}}$ is introduced in Eq. (10), with $A_{\text{nom}} = M \Delta A$. This factor gives an indication of the probability that a crushing bar is surrounded by raising bars, meaning that there is a relative motion at the interface. For a high real area of contact this value is low, representing a low probability that an indented bar is surrounded by raising bars. On the other hand, for a low real area of contact this value is high, representing a high probability that a bar is surrounded by raising bars (although the total number of crushing bars is low for low real area of contacts).

The deterministic variable ω can be regarded as an indentation factor while the deterministic variables ξ, β and ψ can be regarded as internal energy factors. The variable ξ represents the energy required to crush contacting bars, β the energy required to raise non-contacting bars and ψ the energy required to shear bars which have a relative motion to each other. To make an efficient translation from micro to macro contact modeling the deterministic parameters have been described by stochastic parameters in Appendix A. By doing so, all energy factors depend on the statistical parameters U_{L} (raise of bars), d_{L} (separation between the tool surface and the mean plane of the rough surface) and the normalized surface height distribution $\phi_{\text{w}}(z)$ (see Fig. 1). In addition, ω is a function of the normal forces acting on the bars $F_{\text{N}}(z)$. It is noted that an equal raise of bars U_{L} has been assumed, which corresponds to the experimental results of Pullen and Williamson [10].

Balancing the total internal energy (Eq. (5)) with the external energy (Eq. (4)) and introducing the nominal contact pressure p_{nom} defined as $F_{\text{N}}/A_{\text{nom}}$, finally give

$$p_{\text{nom}} = \frac{B}{A_{\text{nom}}} \left(\frac{\xi}{\omega} + \eta \frac{\beta}{\omega} \right) + \frac{S}{A_{\text{nom}}} \frac{\psi}{\omega} \tag{13}$$

2.1.2. Volume conservation

Eq. (13) provides the relation between the nominal contact pressure p_{nom}, the separation d_{L} and the constant raise of the non-contacting surface U_{L}. Another equation is required to compute the separation d_{L} and raise U_{L} for a given normal load p_{nom}. Volume conservation is used for this purpose, which can be written as

$$\sum_{i=1}^{N} \Delta z_i \Delta A = \sum_{l=1}^{N^{**}} \Delta u_l \Delta A + \sum_{j=1}^{N^*} \Delta u_j \Delta A \tag{14}$$

The equation for volume conservation can be written in stochastic form using the stochastic expressions as given in Appendix A

$$A_{\text{nom}} \int_{d_{\text{L}}}^{\infty} (z - d_{\text{L}}) \phi_{\text{w}}(z)\, \mathrm{d}z = A_{\text{nom}} \int_{-\infty}^{d_{\text{L}} - U_{\text{L}}} u(z) \phi_{\text{w}}(z)\, \mathrm{d}z + A_{\text{nom}} \int_{d_{\text{L}} - U_{\text{L}}}^{d_{\text{L}}} (d_{\text{L}} - z) \phi_{\text{w}}(z)\, \mathrm{d}z \tag{15}$$

Taking a constant raise U_{L} of the non-contacting asperities into account, Eq. (15) can be rewritten as

$$U_{\text{L}}(1 - \alpha_{\text{L}}) = \int_{d_{\text{L}} - U_{\text{L}}}^{\infty} (z - d_{\text{L}}) \phi_{\text{w}}(z)\, \mathrm{d}z \tag{16}$$

The separation d_{L} and the raise of the non-contacting surface U_{L} for a given normal pressure p_{nom} can be calculated by solving (Eqs. (13) and 16) simultaneously.

2.2. Flattening due to normal loading + sliding

The normal loading model as discussed in Section 2.1 is adapted to account for sliding effects, which increases the real contact area significantly. The initial value α_{S}^0 is obtained from the normal loading model. The subscript S refers to the influence of sliding on the real contact area.

It is assumed that the increase in real contact area during sliding is caused by two mechanisms. First, the normal loading model assumes contact between a perfectly flat tool surface and a rough workpiece surface, see Fig. 2a. Based on this assumption, energy equations are solved to meet force equilibrium between the applied load and the calculated real contact area. At a smaller scale, however, the tool surface is also rough and the harder tool asperities are penetrating into the softer (crushed) workpiece asperities, see Fig. 2b. If sliding occurs, only the frontal area of a penetrating tool asperity is actually in contact, see Fig. 2c.

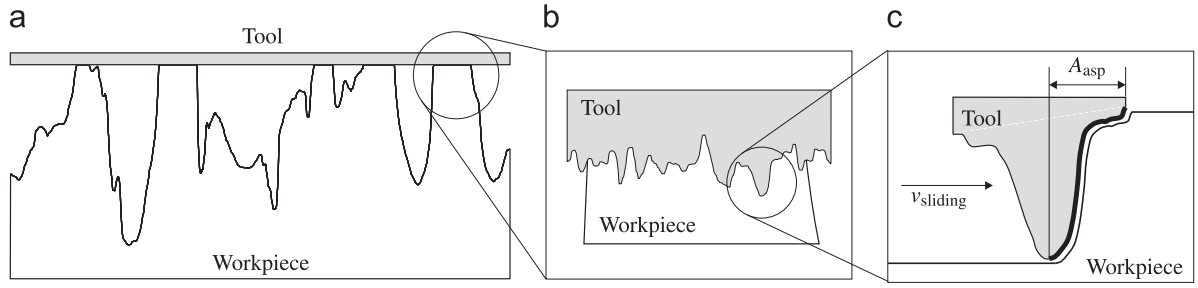

Fig. 2. Schematic view contacting tool asperities. (a) Rough crushed workpiece surface; (b) Zoom-in on rough tool surface; (c) Zoom-in single asperity scale.

Consequently, the real contact area must grow with a factor of approximately 2 in order to satisfy force equilibrium. It is assumed that the following relation holds:

$$\alpha_S^1 = 2\alpha_S^0 \tag{17}$$

Moreover, if asperities are already plastically deformed by a given normal load, they must grow when subjected to an additional tangential load (caused due to sliding). In the literature, this mechanism is known as junction growth [16]. Based on the Von Mises yield criterion, Tabor derived the following relation to account for the influence of tangential loading on the real contact area:

$$\nu = \sqrt{1+\kappa\mu^2} \tag{18}$$

with ν being the increase in fractional real contact area, μ being the friction coefficient and κ being a constant shear factor. For a 3D contact situation there is no theoretical solution for κ and hence, friction experiments are usually executed to determine this value. To find the increase in real contact area ν, an iterative scheme is required since the proposed relation relies on the friction coefficient $\mu(\alpha)$. To find the friction coefficient $\mu(\alpha)$, a deterministic ploughing model is used, as will be discussed in Section 3. Within an iteration step the real contact area is calculated by $\alpha_S^{n+1} = \nu^n \alpha_S^1$, by which the friction coefficient $\mu(\alpha_S)$ will change in the next iteration. The iterative procedure is repeated until $|\alpha_S^{n+1} - \alpha_S^n| < e$, where e is a predefined error threshold. If the error threshold is satisfied, the indentation d_S and raise of the surface U_S is solved from the definition of the real contact area (Eq. (A.6)) and volume conservation (Eq. (16)). A Newton Raphson procedure is used for this purpose. U_S and d_S are subsequently used to account for the effect of bulk deformation on the real contact area, Section 2.3.

2.3. Flattening due to combined normal loading and stretching

When asperities are already in a plastic state under normal loading, only a small stress in the underlying bulk material (perpendicular to the loading direction) initiates further plastic deformation of asperities. As a result, more indentation of contacting asperities will occur and hence, the real contact area will increase. In the literature, this is known as the decrease in effective hardness due to bulk straining of the underlying material [34,12,13]. The effective hardness H_{eff} is defined as

$$H_{\text{eff}} = \frac{p_{\text{nom}}}{\alpha} \tag{19}$$

Westeneng [8] derived an analytical contact model to describe the influence of bulk straining on deforming, arbitrarily shaped, asperities. Analogue to the normal loading model, this model considers contact between a flat hard surface and a soft rough surface. Plastic material behavior is assumed without work-hardening effects. The outcomes of the sliding model (U_S, d_S and α_S), as discussed in the previous section, are used as the initial values for U_ε^0, d_ε^0 and α_ε^0. The subscript ε indicates the variables that are bulk strain dependent.

Westeneng derived the following relation to describe the change in fractional real contact area α_ε as a function of the in-plane strain ε_p:

$$\frac{d\alpha_\varepsilon}{d\varepsilon_p} = lW\frac{d\alpha_\varepsilon}{d(U_\varepsilon - d_\varepsilon)} \tag{20}$$

with l being the mean half spacing between asperities:

$$l = \frac{1}{2\sqrt{\rho_w \alpha_\varepsilon}} \tag{21}$$

in which ρ_w describes the asperity density of the workpiece surface. The definition for l is approximately true for surfaces with no particular roughness distribution.

Sutcliffe [13] performed slip-line analysis to describe the deformation of wedge-shaped asperities under combined normal loading and straining of the underlying bulk material. Based on slip-line results, Sutcliffe showed the relation between the velocity parameter W and the characteristic slip-line angle γ. γ is bounded by $0 \le \gamma \le \pi/2$ due to geometrical conditions. The expression of the slip-line angle is given by [13]

$$\gamma = \frac{H_{\text{eff}}}{4k}(1-\alpha_\varepsilon) \tag{22}$$

with k being the shear strength of the workpiece material. The expression for k follows from the Von Mises yield criterion under pure shear, and is defined as $k = H/B\sqrt{3}$. H is the initial hardness of the material and B represents the hardness factor as discussed in Section 2.1. Based on the slip-line results presented in [13], Westeneng proposed in [8] the following semi-empirical relation to describe the velocity parameter W as a function of the fan angle γ

$$W = -0.184 + 1.21\exp(1.47\gamma) \tag{23}$$

The definition of the fractional real contact area (Eq. (24)) is used to solve the differential equation in the right-hand side of Eq. (20), see Eq. (25):

$$\alpha_\varepsilon = \int_{d_\varepsilon - U_\varepsilon}^{\infty} \phi_w(z)\,dz \tag{24}$$

$$\frac{d\alpha_\varepsilon}{d(U_\varepsilon - d_\varepsilon)} = \frac{d}{d(U_\varepsilon - d_\varepsilon)}\int_{d_\varepsilon - U_\varepsilon}^{\infty} \phi_w(z)\,dz = \phi_w(d_\varepsilon - U_\varepsilon) \tag{25}$$

Substituting Eq. (25) into Eq. (20) yields

$$\frac{d\alpha_\varepsilon}{d\varepsilon_p} = lW\phi_w(d_\varepsilon - U_\varepsilon) \tag{26}$$

To calculate the change in α_ε, the value of U_ε and d_ε needs to be solved simultaneously while ε_p is incrementally increased. Based on volume consistency and the fractional real contact area, α_ε, U_ε and d_ε can be obtained by using a Newton Raphson procedure. For readability purposes, the subscript ε will not be used in the remainder of this paper, hence $\alpha = \alpha_\varepsilon$, $U = U_\varepsilon$ and $d = d_\varepsilon$.

3. Determination of friction coefficient

Ma et al. [29] proposed a contact model that accounts for tool asperities forming contact patches under high fractional real contact areas. The model of Ma was originally developed for extrusion processes, and is adapted to describe friction in sheet metal forming. A deterministic description of the rough workpiece and tool surface is accounted for, in contrary to the stochastic description as used in the deformation models described in Section 2. The contact model of Challen and Oxley [24,25] is used to predict friction forces acting on individual contact patches, Section 3.1. The model of Ma et al. is discussed in Section 3.2 to describe the formation of contact patches between contacting surfaces. Finally, the total friction force is obtained by the individual contributions of all contact patches, see Section 3.3.

3.1. Single asperity friction model

Friction forces acting on individual contact patches are described by adopting the contact model of Challen and Oxley [24,25]. Challen and Oxley deduced 2D slip-line fields, assuming a plane strain deformation state and ideal-plastic material behavior. The authors proposed relations describing the steady-state friction between a wedge-shaped asperity indenting into a softer flat counter surface under cutting, ploughing and wear conditions. The active mode can be determined by the so-called wear-mode diagrams [35,24]. These diagrams describe the friction modes as a function of the attack angle of a wedge-shaped asperity θ and the shear factor f_C, where the latter describes the shear strength of the interfacial boundary layer over the shear strength of the plastic deforming material (the workpiece material). A mathematical description of all regimes is required since different contact conditions occur during metal forming.

The cutting regime applies to sharp asperities that cause material to be removed in the form of chips and therewith creating a groove in the softer material. The expression for the friction coefficient μ in the cutting regime is given by Challen and Oxley in [24]:

$$\mu_{\text{cutting}} = \tan\left(\theta - \tfrac{1}{4}\pi + \tfrac{1}{2}\arccos(f_C)\right) \tag{27}$$

Ploughing is caused by blunt asperities causing material to shift to the sides of the created groove, expressed by Eq. (28) [24]:

$$\mu_{\text{ploughing}} = \frac{A_1 \sin\theta + \cos(\arccos(f_C - \theta))}{A_1 \sin\theta + \sin(\arccos(f_C - \theta))} \tag{28}$$

with

$$A_1 = 1 + \frac{1}{2}\pi + \arccos(f_C) - 2\theta - 2\arcsin\left(\frac{\sin(\theta)}{(1-f_C)^{1/2}}\right) \tag{29}$$

The wear regime is characterized by removal of deformed material producing wear particles. The expression for the friction coefficient in this regime is given in [24]:

$$\mu_{\text{wear}} = \frac{\{1 - 2\sin A_2 + (1-f_C^2)^{1/2}\}\sin\theta + f_C\cos\theta}{\{1 - 2\sin A_2 + (1-f_C^2)^{1/2}\}\cos\theta - f_C\sin\theta} \tag{30}$$

with

$$A_2 = 1 - \frac{1}{4}\pi - \frac{1}{2}\arccos f_C + \arcsin\left(\frac{\sin\theta}{(1-f_C)^{1/2}}\right) \tag{31}$$

The value of the attack angle θ is determined based on the contact model proposed in the next section. The shear factor f_C is defined as τ/k. τ describes the shear strength of the interfacial boundary layer and k the shear strength of the plastic deforming material. The boundary layer shear strength τ is described by the following form:

$$\tau = C\left(\frac{p}{p_0}\right)^n \tag{32}$$

with the shear strength τ and the constant C in Pa. p describes the applied contact pressure and p_0 the reference pressure in Pa. Since full plasticity is assumed during ploughing, the contact pressure p equals the hardness H of the softer material, i.e. $\tau = C(H/p_0)^n$. An experimental procedure to obtain the parameters C and n is presented in detail in [36].

3.2. Multiple asperity friction model

The multiple asperity friction model relies on the projection of two deterministic rough surfaces onto each other. Since the model makes use of one-to-one pixel mapping, both surfaces should be equal in size and resolution. The surface texture of the virgin workpiece material is adapted for the amount of flattening and raise of asperities, which is calculated from the flattening models discussed in Section 2. The plateaus of the flattened workpiece asperities are assumed to be perfectly flat, in which the harder tool asperities are penetrating. The separation between the mean plane of the tool surface and the flattened peaks of the workpiece surface is calculated based on force equilibrium, obtained by the summation of the load carried by the formed contact patches.

Contact patches are determined by binary image processing techniques. A contact patch is identified by a cluster of pixels (penetrating into the softer counter surface) connected together by either sharing pixel edges or by sharing pixel edges and pixel corner points, see Fig. 3a. An elliptical paraboloid is fitted through the height data of the contact patch to determine the attack angle of the contact patch in sliding direction (see Fig. 3b and c). The geometrical characteristics of the equivalent contact patch are indicated in Fig. 3c.

The base of the elliptical paraboloid is approximated by an ellipse having the same normalized second central moments as the combined pixels of the patch [37], which is a common technique used in image processing. The geometrical parameters defining this ellipse are the major axis a and the minor axis b at

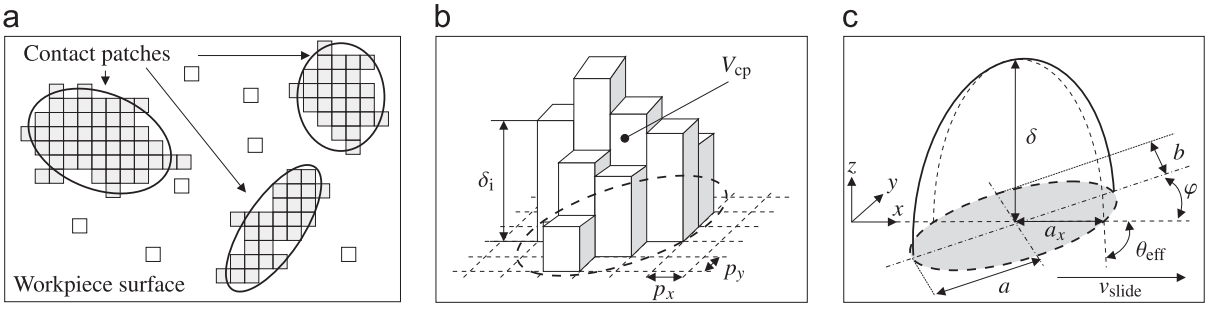

Fig. 3. Schematic view contact patches [29]. (a) Definition contact patches; (b) Volume of a contact patch; (c) Geometrical characteristics.

the penetration depth δ, and the orientation angle φ between the horizontal and the major axis of the ellipse (see Fig. 3c).

The volume V_{ell} of the elliptical paraboloid, indented a distance δ into the softer counter surface, is defined as

$$V_{ell} = \int_0^{\delta} \pi a'(z) b'(z)\, dz = \int_0^{\delta} \frac{\pi ab(\delta - z)}{\delta} z\, dz = \frac{\pi ab\delta}{2} = \frac{A_{ell}\delta}{2} \tag{33}$$

with $a'(z) = a\sqrt{(\delta - z)/\delta}$ and $b'(z) = b\sqrt{(\delta - z)/\delta}$ being the major and minor axis of the elliptical paraboloid as a function of z respectively. The area of the base ellipse is $A_{ell} = \pi ab$. The height δ of the elliptical paraboloid is calculated such that the volume and contact area of the representative paraboloid are the same as the actual contact patch:

$$\delta = \frac{2V_{ell}}{A_{ell}} = \frac{2V_{cp}}{A_{cp}} = \frac{2p_x p_y \sum_{i=1}^{n} \delta_i}{n p_x p_y} = \frac{2}{n} \sum_{i=1}^{n} \delta_i \tag{34}$$

with n being the number of discrete surface points spanned by the contact patch and p_x and p_y being the pixel size of the rough tool surface. The suffix 'ell' refers to the elliptical paraboloid, the suffix 'cp' refers to the discrete contact patch.

The effective attack angle θ_{eff} between the elliptical paraboloid and the counter surface, see Fig. 3c, is defined as

$$\theta_{eff} = \arctan\left(\frac{2\delta}{a_x}\right) \tag{35}$$

in which $2\delta/a_x$ is the tangent of the elliptical paraboloid in the direction of sliding (at $z=0$). The characteristic length a_x relies on the geometry and orientation of the elliptical paraboloid, expressed by

$$a_x = \frac{ab}{\sqrt{(b\cos\varphi)^2 + (a\sin\varphi)^2}} \tag{36}$$

From which the definition for the effective attack angle can be obtained as

$$\theta_{eff} = \arctan\left(\frac{2\delta\sqrt{(b\cos\varphi)^2 + (a\sin\varphi)^2}}{ab}\right) \tag{37}$$

The attack angle is used to obtain the friction force acting on one contact patch according to Challen and Oxley. The model of Challen and Oxley describes ploughing and adhesion effects in a 2D plane strain expression, interpreting the effective attack angle θ_{eff} as an infinite cylinder. A translation is therefore required to capture the 3D nature of the contact patch into a 2D expression. To satisfy this requirement, Hokkirigawa and Kato [35] introduced the shape factor χ to modify the effective attack angle θ_{eff}, see Eq. (38). They found values of $\chi = 0.8$ by indenting a spherical shaped indenter into brass, carbon steels and austenitic stainless steels. However, sliding experiments should be executed for every unique tool–workpiece combination for a reliable determination of the shape factor χ [35]:

$$\theta = \arctan\left(\frac{2\delta\sqrt{(b\cos\varphi)^2 + (a\sin\varphi)^2}}{\chi ab}\right) \tag{38}$$

3.3. Calculation of friction coefficients

The aforementioned procedure is carried out for all contact patches between the workpiece and the tool surface. Knowing the effective attack angle of each contact patch in the direction of sliding, the total friction force becomes the summation of all individual contributions. The coefficient of friction is obtained by dividing the total friction force by the total load carried by the contact patches:

$$\mu = \frac{F_W}{F_N} = \frac{\sum_{i=1}^{m} \mu_i(\theta_i) A_i H}{\sum_{i=1}^{m} A_i H} \tag{39}$$

with m being the number of contact patches and μ_i being the friction coefficient of a single contact patch. The friction coefficient μ_i is described by (Eqs. (27), 28) or (30), depending on the attack angle θ (Eq. (38)) and the shear factor f_C.

The anisotropy of contact patches is captured by this approach as well. That is, if a different orientation of asperities is used, the shape of the elliptical paraboloids will change. For isotropic surfaces, one would expect circular shaped base ellipses ($a \approx b$). For anisotropic surfaces, however, ellipses with a higher ellipticity ($a > b$) can be expected. This means that the direction of sliding has an influence on the evaluated friction coefficient. Therefore, a direction dependent friction coefficient can be obtained by this friction model, which depends on the asperity orientation of both the tool and the workpiece surface.

4. Model parameter determination

The accuracy of the boundary lubrication friction model depends on a proper determination of input parameters. An experimental method is presented in Section 4.1 to measure representative 3D rough surface textures. Input parameters of the micro-mechanical friction mechanisms discussed in Sections 2 and 3 are obtained by calibrating model results to experimental results. The real contact area is used in Section 4.2 to quantify parameters introduced by the normal loading models, the friction coefficient is used to obtain parameters introduced by the ploughing model. Normal loading + stretching is not discussed in this section as no empirical parameters have been introduced in the stretching model. It is, however, noted that this model has been experimentally verified by Westeneng in [8] and numerically validated by Hol et al. in [4] and in [36]

4.1. Surface parameters

The boundary lubrication friction model requires both a deterministic description and a stochastic description of the tool and the workpiece surface.

3D surface scans are obtained by confocal microscopy measurements. Fig. 4a and b shows a surface measurement on electro discharged textured (EDT) sheet material and on a ground tool surface. Measured surface textures must be corrected on two aspects before they can be used for a friction analysis. First, errors are introduced during the measurement represented by sharp peaks, called spikes. A noise filter is required to remove these spikes from the measurement data. A filter often used in the field of image and signal processing is the median filter, a non-linear digital filtering technique [38]. The results discussed in this paper have been obtained by using a kernel size of 3, meaning that a matrix of 3×3 points is used to determine the median of each point. Second, a tilt or curvature might be present in the measured surface texture due to the geometry of the specimen, or due to misalignments of the specimen during the measurements. The surface measurement should be corrected for these two aspects since perfectly aligned surfaces are required to perform a friction analysis. For this purpose, a 2nd order polynomial function is fitted through the measurement data. The measurement data is shifted, tilted and straightened to its origin by subtracting the polynomial function from the measurement data. Corrected surfaces of both the workpiece and the tool material are shown in Fig. 4a and b.

Moreover, a representative surface scan of both the tool material and the workpiece material is required. Representative

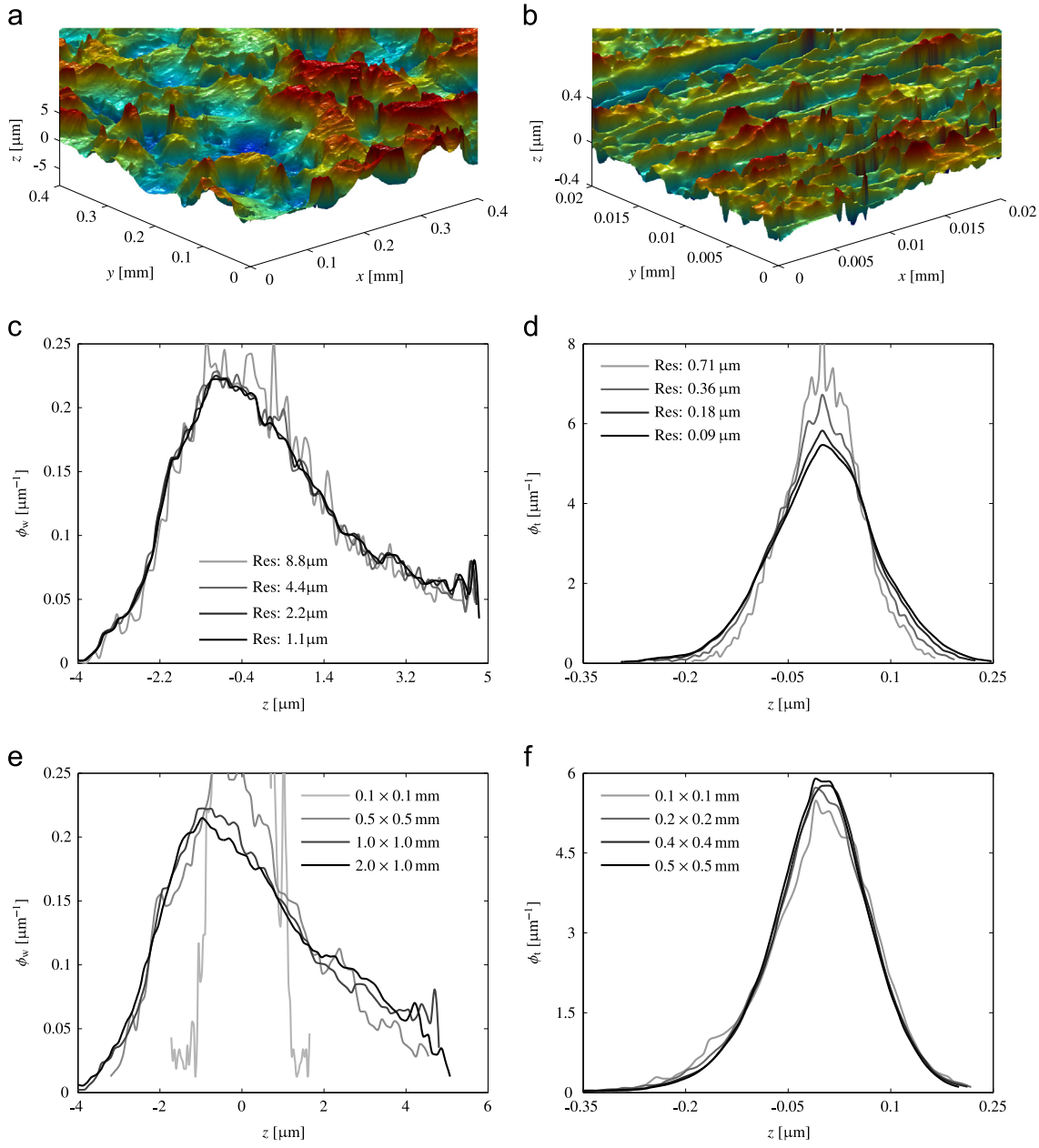

Fig. 4. 3D surface impression measured by confocal microscopy (a–b), height distributions for different pixel sizes (c–d) and height distributions for different measurement areas (e–f).

means that a resolution is used which is fine enough, while the size of the measurement area is large enough, to capture the most important details of the surface. The representativeness of a surface measurement is related to the surface height distribution in this section. That is, given a finer resolution and a larger measurement area the shape of a surface height distribution will converge. For computational purposes, the measurement size and pixel size is used for which the shape of the surface height distribution is close to the converged shape.

Fig. 4c shows surface height distributions of the workpiece surface for 4 different pixel sizes, using a measurement area of 1 × 1 mm. It is observed that the difference in surface height distributions is small for pixel sizes less than 2.2 μm. Hence, a pixel size of 2.2 μm is used in this paper. Fig. 4e shows surface height distributions for 4 different area sizes. It is concluded that a measurement area of 1 × 1 mm captures enough detail to ensure a representative surface scan of the workpiece. The same analysis has been performed on the tool surface, see Fig. 4d and f for the pixel size comparison and measurement area size comparison, respectively. A maximum pixel size of 0.18 μm and a minimum measurement area of 0.4 × 0.4 mm ensure a representative surface scan of the tool surface. However, due to computer resources, a pixel size of 0.36 μm and an area of 0.4 × 0.4 mm are used. The difference in measurement area and scanning resolution between the tool surface and the workpiece surface is caused by the difference in roughness values. Hence, the relatively smooth tool surface ($S_q = 0.06$ μm) allows a smaller measurement area and requires a finer scanning resolution than the rougher workpiece surface ($S_q = 1.9$ μm).

The asperity deformation models discussed in Section 2 depend on a stochastic description of the rough workpiece surface. This means that the surface height distribution of the workpiece ϕ_w is used to make an efficient translation from micro-scale contact modeling to macro-scale contact modeling. Moreover, to

describe flattening of asperities due to combined normal loading and straining of the underlying bulk material the asperity density ρ_w is required.

The surface height distribution is obtained from 3D rough surface measurements. Various methods exist to describe surface height distributions by continuous functions, which is desirable for efficiency reasons. Often a normal distribution function is used. However, the surface height distribution of the undeformed material is usually asymmetric, requiring a more advanced method to approximate the surface height distribution. By using B-splines [39,40], asymmetric surface height distributions can be approximated. The accuracy of the approximation depends on the order of the splines and the number of splines used to construct the curve. The B-spline function is used in this work to approximate surface height distributions, for which 15 cubic splines have been used.

The second stochastic parameter is described by the asperity density ρ_w. The location of asperities can be obtained by using a 3-point summit rule (for 2D line profiles) or using a 9-point summit rule (for 3D surfaces) [41]. A summit refers to the tip of an asperity, and is defined as a surface point which is higher than its neighboring points. If the location and number of summits are known, the asperity density can be obtained.

For the results discussed in this paper an exponential relation has been used to express the asperity density as a function of the nominal contact pressure [36], see Eq. (40) with p_{nom} in MPa. That is, the asperity density decreases for increasing nominal contact pressures, as asperities are joining together under high fractional real contact areas. Since the asperity density is a property of the surface the coefficients given in Eq. (40) only hold for the workpiece material as discussed in this paper:

$$\rho_w = 1.49 \times 10^3 \exp(-0.458 p_{nom}) + 3.14 \times 10^2 \exp(-0.0460 p_{nom}) \quad (40)$$

4.2. Parameter calibration

The reference parameter λ, the shear factor κ and the shape factor χ will be calibrated using a Rotational Friction Tester (RFT), developed at Tata Steel [21]. Experiments have been conducted at room temperature, excluding possible temperature effects on friction [42,43]. It is, however, noted that the influence of temperature could be accounted for by introducing temperature dependent relations in (Eqs. (1) and 32), and by conducting the experiments as discussed in this section under elevated temperatures.

The RFT consists of a stationary punch and a rotating workpiece holder, see Fig. 5a. The workpiece holder is driven by a computer controlled brushless servo drive with a low inertia reduction gear. The punch consists of 3 small notches having a flat polished contact area, aligned in one plane and positioned at the same radius from the center of the punch. The tool is pressed on the workpiece by a hydraulic actuator. The applied load to the workpiece and induced torque due to sliding are measured by a load/torque transducer. The feasible pressure range applied to the notches depends on the nominal contact area of these notches. By using a tooling with larger or smaller notch areas, the feasible pressure range can be decreased or increased, respectively. The tool is rotated over a user defined rotation angle after applying the load. The conditions of the tests are listed in Table 1.

For the normal loading only case, the tool was pressed on the workpiece till a specific pressure was reached. To investigate the development in real contact area, pre-defined locations on the workpiece have been scanned by 3D confocal microscopy before and after the loading experiments. Fig. 5b shows an example of the workpiece and the location of confocal measure-

Table 1
Process specifications RFT.

Parameter	Specification
Blank material	DC06 EN10130:2006
Tool material	DIN 1.2379
Lubricant	Quaker FERROCOAT ® N6130
Lubrication amount	0.6 g/m^2
Notch size	8 × 8 mm
Punch center-notch radius	46 mm
Workpiece size	120 × 120 mm
Speed	10 mm/s
Pressure	10,20,30,45,60 MPa
Sliding angle	80°/ 120°

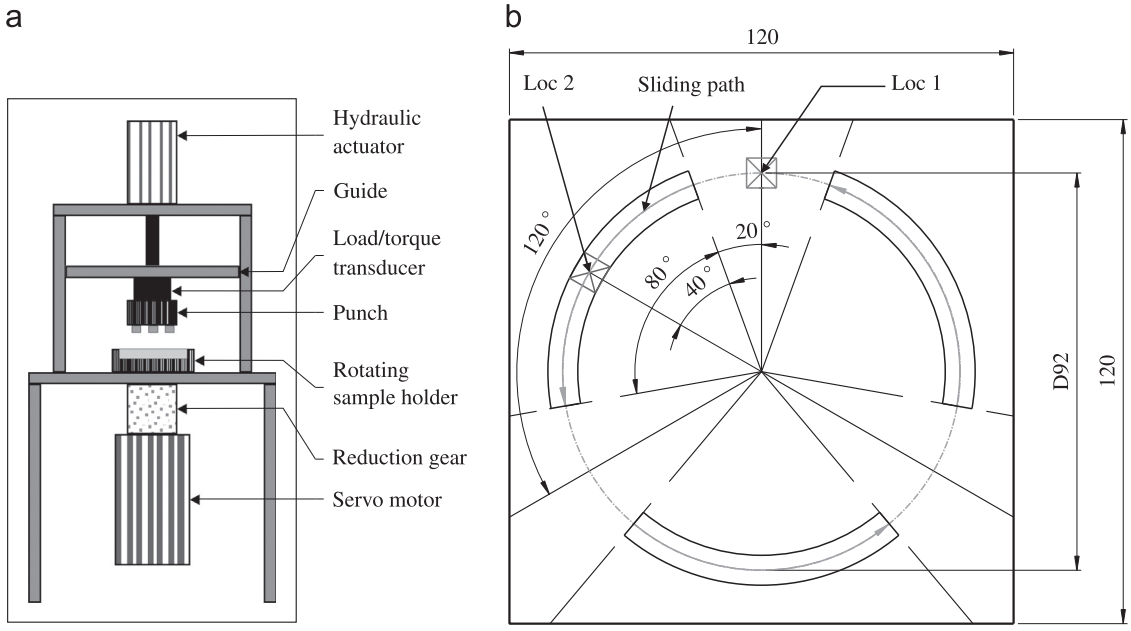

Fig. 5. Impression RFT test set-up. (a) Rotational friction tester. (b) Workpiece sample for loading/sliding experiments.

ments, indicated by 'Loc 1'. Measurements are performed on the same location within an accuracy of 1 μm.

In the case of normal loading + sliding, the tool was rotated 20° with respect to the normal loading position (Loc 1), and subsequently loaded and slided over a sliding angle of 80°. 'Loc 2' in Fig. 5b indicates the position where confocal measurements have been performed.

Fig. 6a and b presents 3D measured surface textures showing sliding-induced asperity deformation. The surface shown in Fig. 6b experienced sliding under a load of 60 MPa in the negative y direction. A significant amount of asperity deformation is observed. Shallow ploughing tracks of the tool asperities are clearly visible, e.g. the highlighted section in Fig. 6a and b.

A top view and cross sections of both the deformed and undeformed surfaces are shown in Fig. 6c and d respectively. Fig. 6c shows the undeformed surface asperities (gray) projected on the flattened plateaus of the deformed surface asperities (black). For this purpose, a threshold height equal to the amount of deformation of the deformed surface has been used to cut-off the undeformed surface asperities. By doing so, the black areas visualize the deformation of surface asperities in the x and y directions compared to the cross-sectional area of the undeformed asperities. Fig. 6d shows cross sections in the x and y directions of the undeformed (gray) and deformed surface (black). Contact spots are indicated by locations where asperities have been flattened. It can be observed that asperities are smeared out in sliding direction (negative y direction).

Fig. 6e and f shows the initial surface height distributions (dashed lines) and the surface height distributions of the deformed surfaces (solid lines) for normal loading and sliding a surface with 60 MPa. Fig. 6e corresponds to the normal loading only case, Fig. 6f corresponds to the normal loading + sliding case.

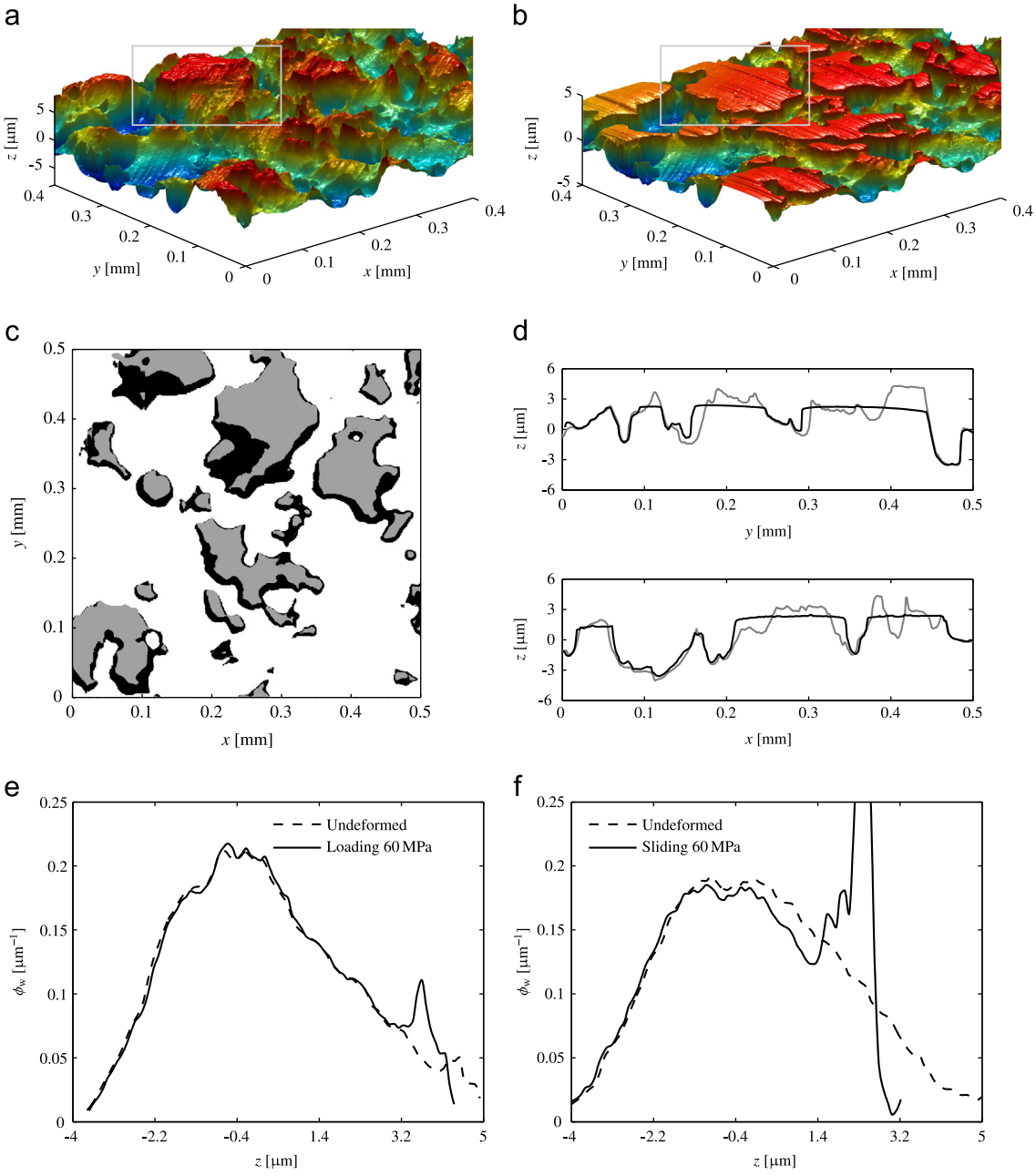

Fig. 6. 3D measured surface textures of the workpiece surface (a–b), indication direction and amount of surface deformation (c–d) and undeformed and deformed surface height distributions for normal loading and sliding a surface with 60 MPa (e–f).

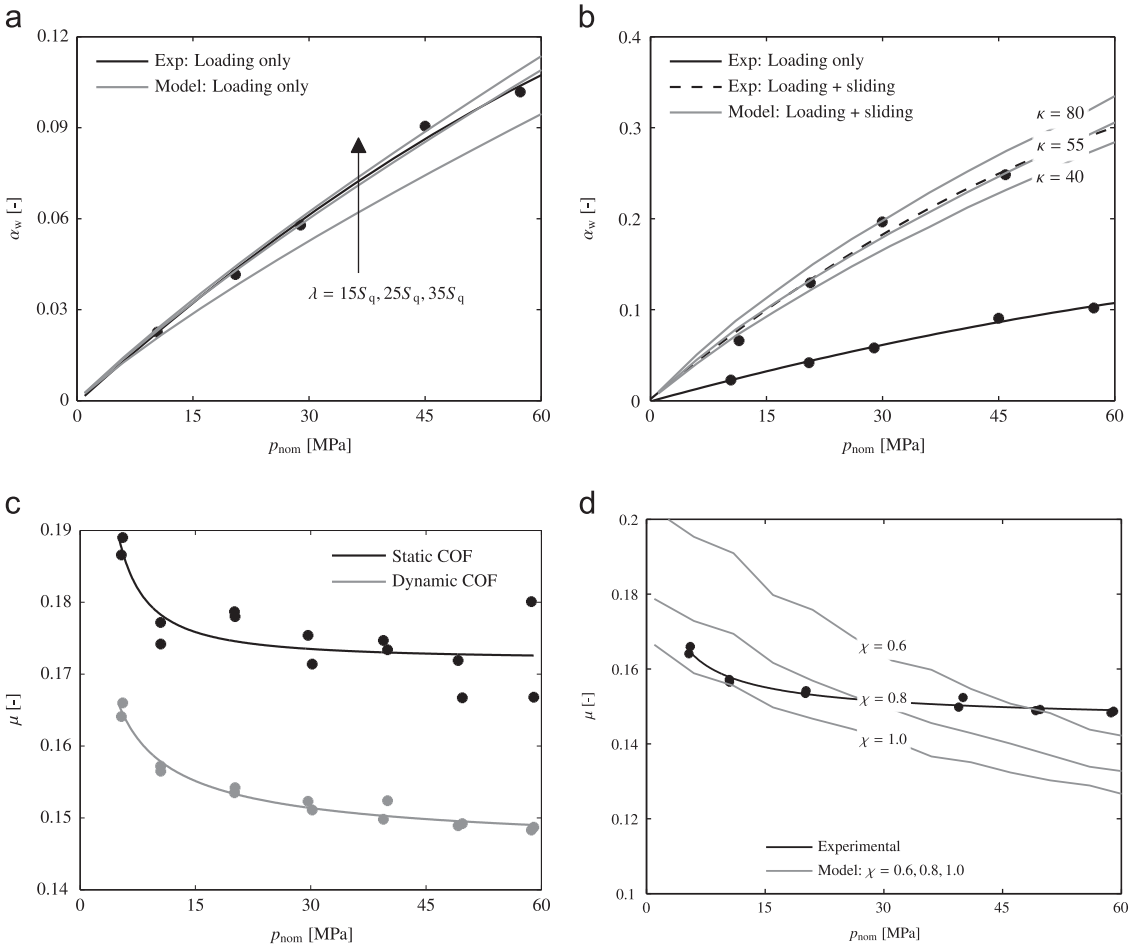

Fig. 7. Development real contact area α_w due to normal loading and normal loading + sliding (a–b), the development in static and dynamic friction coefficients as a function of nominal contact pressure (c) and a comparison between experimentally and numerically obtained friction coefficients (d).

For both cases, a peak is visible at the location where asperities have been flattened by the tool. The height of the peak indicates the amount of deformed surface points. The width of the peak refers to the combined effect of tool asperity indentation and springback of the crushed workpiece asperities after releasing the tool from the workpiece. Since the surface height distributions have been normalized, the area underneath the initiated peak is used as a measure for the fractional real contact area α_w. This fraction reflects the ratio between the surface points which have been in contact with the tool and the total number of surface points.

The fractional real contact area is determined by calculating the area underneath the peak caused by deformation, starting from the start of the peak till the right end of the curve. The relation between nominal contact pressure and fractional real contact area is shown in Fig. 7b for both normal loading only and normal loading + sliding cases. Experimental results are expressed by dots, the overall trend is fitted by a 2nd order polynomial function (the black lines). It can be seen that the influence of sliding on the fractional real contact area is significant. An increase by a factor of 3 is found over the complete range of nominal contact pressures. For both cases, non-linear behavior of the real contact area as a function of the loading/sliding pressure is observed. The non-linearity is induced by work-hardening effects of the deformed asperities, resulting in a lower than proportional increase in real contact area with nominal contact pressure [21].

The reference parameter λ, which was introduced in Eq. (2) to account for work hardening effects, is used to fit the normal loading model to the experimental results.[1] Results using different values for λ are shown in Fig. 7a. The value of λ has been expressed as a function of the RMS surface roughness parameter S_q. It can be observed that the trend in fractional real contact area can be predicted accurately when using a value of $\lambda = 25S_q$ (mean error = 1.4% compared to the trend line).

The contact model proposed in Section 2.2 accounts for the increase in real contact area due to sliding of contacting surfaces. This model introduced the shear factor κ, which modifies the calculated tangential load between the contacting surfaces. The value of κ is usually determined based on experiments [17,19,44]. In this work, the real contact area obtained from normal loading + sliding experiments is used to find a proper value of κ. The influence of κ on the real contact area is shown in Fig. 7b. An accurate prediction of the development in real contact area is obtained if a value of 55 is used (mean error = 1.5% compared to the trend line).

Finally the shape factor χ has to be fitted. The rotational friction tester has been used to obtain the relation between the friction coefficient and the applied nominal contact pressure. The friction coefficient is derived from the measured load and torque, obtained from the load/torque transducer. Experiments have been conducted for different constant loading conditions. The static and

[1] From the confocal study, the raising of non-contacting asperities seems negligible for this particular situation. Hence, the accompanying energy to lift these asperities is negligible in this case as well. For simplicity reasons, the persistence parameter is set to 0 when fitting λ.

dynamic friction coefficients as a function of nominal contact pressure are shown in Fig. 7c. The markers show the experimental values, the solid lines represent trend lines (based on a 2nd order power law). The dynamic friction coefficient equals the averaged value of the friction coefficient between a sliding angle of 20° and 100° in the RFT. Both the static and dynamic friction coefficients decrease with increasing nominal contact pressure. This behavior agrees with observations on coated steels by Emmens [21], on coated and uncoated steels by Schedin [45] and on different steel grades and aluminum alloys by Roll et al. [46] and Filzek et al. [47]. The decrease in friction coefficients can be explained by the ploughing model, as will be discussed in Section 5.

The effect of χ on the calculated dynamic friction coefficients is visualized in Fig. 7d. Decreasing the shape factor χ increases the effective attack angle, resulting in higher friction coefficients. Comparing analytical with experimental results shows that experimental results can be predicted best by using a value of $\chi = 0.8$ (which corresponds to the experimental value obtained by Hokkirigawa and Kato in [35]). Although the calibrated model overestimates the negative correlation between the friction coefficient and the nominal contact pressure, the calculated friction coefficients are within the expected range of experimentally obtained friction coefficients.

5. Application to forming processes

Two deep-drawing applications have been used to demonstrate the applicability of the developed boundary lubrication friction model to metal forming processes, i.e. a top-hat section and a cross-die product (see Fig. 8). From practice it is known that starvation of lubricant occurs in case a lubrication amount of 0.6 g/m^2 is used, meaning that only boundary lubrication friction takes place. To obtain friction in the boundary lubrication regime, experiments have therefore been performed using a lubrication amount of 0.6 g/m^2.

Two strategies can be chosen for the implementation of the boundary lubrication friction in FE software. One way is to implement the friction model directly into the FE code, and solve the friction model once a node of the workpiece contacts the tool surface. However, this will yield a significant increase in computation time since all equations have to be solved for each node in contact, for every time step of the FE simulation. A computationally more efficient approach is to construct a friction matrix for a predefined range of nominal contact pressures exerted on the surface and strains occurring in the bulk material. This friction matrix can be used as a look-up table in an FE simulation. An additional advantage of this approach is the possibility to generate friction matrices for specific metal–lubricant combinations. That is, as the friction model accounts for material properties, lubricant properties and surface characteristics, different metal–lubricant combinations will result in different friction matrices. A friction matrix has to be constructed only once for such a specific combination, after which it can be used to describe friction in different FE forming simulations.

For the two applications discussed in this paper the same metal–lubricant combination was used and the tooling was prepared identically (the same surface characteristics). As a result, a friction matrix has been constructed only once and used in both FE simulations. Fig. 9a shows calculated friction coefficients for a pressure range of 1–60 MPa using a bulk strain of 0, 0.1, 0.2 and 0.3. The non-smooth development of friction coefficients is introduced by the deterministic nature of the ploughing model. Increasing the nominal contact pressure p_{nom} or increasing the bulk strain ε both result in decreasing friction coefficients, which can be attributed to the increase in real contact area, see Fig. 9b. Contact patches are joining together for increasing real contact areas resulting in a decrease in effective attack angles and a decrease in the number of active contact patches. Smaller attack angles yield less resistance against sliding, resulting in lower friction coefficients.

The strain in the bulk material is obtained by shell or solid elements during the forming simulation, and is subsequently used to find nodal friction coefficients from the friction matrix. The nominal contact pressure is calculated by the contact algorithm of the FE software.

For the FE simulations, the workpiece was meshed with triangular discrete Kirchhoff shell elements using 3 integration points in plane and 11 integration points in thickness direction. Only a quarter of the product was modeled due to symmetry. The tools are assumed rigid. The yield surface of the blank material was described by the Vegter model [32] using the Bergström–Van Liempt hardening relation [48]. Material parameters used to describe the yield curve and hardening relation are given in Table 2.

5.1. Top-hat section

The top-hat section (Fig. 8a) is formed by a strip drawn into a simple U-shaped profile and is used in practice to, among other things, establish the lubricating behavior of lubricants on (coated and uncoated) blanks under realistic forming conditions. The top-hat tooling consists of a punch, a die and a blankholder. The radii of the die shoulder and the punch shoulder are 4 mm and 5 mm, respectively. The punch has a width of 40 mm, the blankholder and die have a width of 48 mm. Strips of 300 × 25 mm with a thickness of 0.8 mm have been used. The punch stroke has been set to 75 mm. The process specifications are listed in Table 3. Experiments have been conducted using different blankholder forces.

Fig. 10a shows a contour plot of friction coefficients at 55 mm punch displacement. Results are shown for the lower side of the

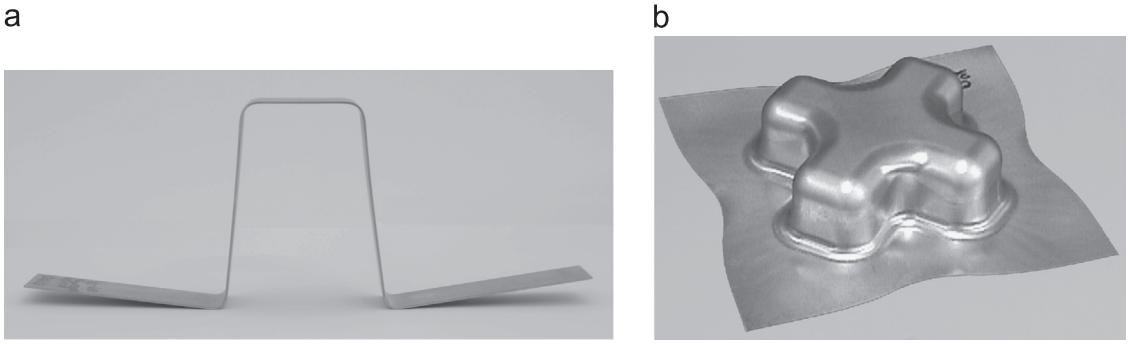

Fig. 8. Pictures of metal forming processes discussed in this paper. (a) Top hat section. (b) Cross-die product.

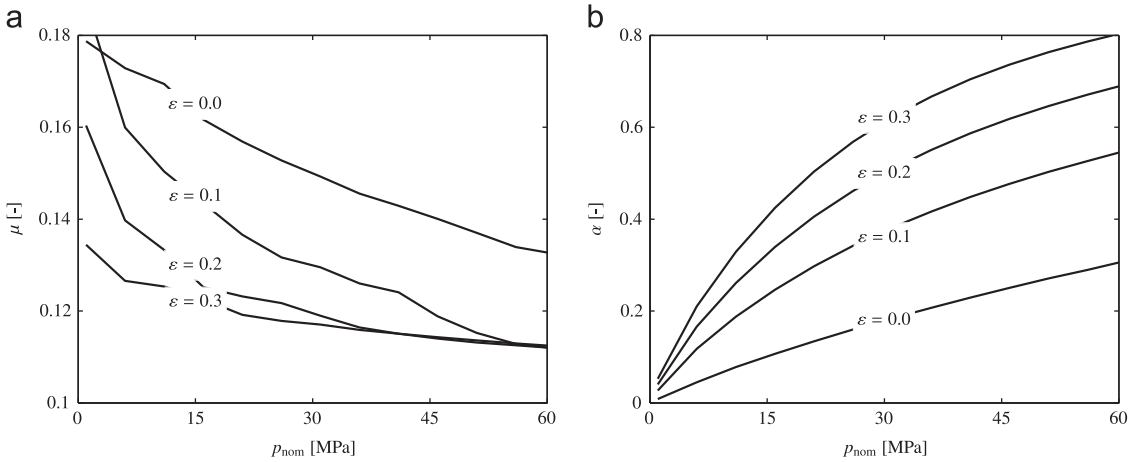

Fig. 9. (a) Development of the friction coefficient for different bulk strains. (b) Development of the real contact area for different bulk strains.

Table 2
Vegter parameters and Bergström–Van Liempt hardening parameters for DC06.

Vegter parameter	0°	45°	90°
R-value	1.85	2.06	2.51
Uniaxial factor (f_{un})	1.0	0.9947	0.9931
Plane-strain factor (f_{ps})	1.2427	1.2476	1.1456
Plane-strain ratio (α)	0.5	0.5	0.5
Pure shear factor (f_{sh})	0.5720	0.5421	0.5002
Equi-biaxial factor (f_{bi})	1.1530		
Equi-biaxial ratio (ρ_{bi})	0.7770		
Hardening parameter	Value		Unit
Initial static stress (σ_{f0})	101.47		MPa
Stress increment parameter ($d\sigma_m$)	251.83		MPa
Linear hardening parameter (β_v)	0.5		
Remobilization parameter (ω)	9.951		
Hardening exponent (n)	0.75		
Initial strain (ε_0)	0.005		
Initial strain rate ($\dot{\varepsilon}_0$)	10^8		
Max. dynamic stress (σ_0^*)	600		MPa
Temperature (t)	300		K
Dynamic stress power (p)	2.2		
Activation energy (ΔG_0)	0.8		J
Boltzmann's constant (k)	8.617×10^{-5}		eV

Table 3
Process specifications top-hat section and cross-die product.

Parameter	Specification
Blank material	DC06 EN10130:2006
Tool material	DIN 1.2379
Lubricant	Quaker FERROCOAT ® N6130 ($\eta_{40^\circ} = 23$ mPas)
Lubrication amount	0.6 g/m^2
Specific parameters top-hat:	
Blank geometry	$300 \times 25 \times 0.8$ mm
Blankholderforce (F_{bhf})	10 kN, 17.5 kN and 25 kN
Punch velocity (v_{punch})	20.0 mm/s
Drawing depth	75 mm
Specific parameters cross-die:	
Blank geometry	$260 \times 260 \times 0.8$ mm
Blankholderforce	120 kN, 150 kN and 170 kN
Drawing velocity	25 mm/s
Drawing depth	60 mm

blank, representing the side of the blank in contact with the die. The gray area indicates that there is no contact, hence no friction coefficients are calculated for this region. Zooming-in on the contact zone shows a variation in friction coefficients from the flat die region towards the die shoulder. The evolution of friction coefficients is mainly dominated by the variation in nominal contact pressures within this region, since strains within the blank are relatively low. The evolution of friction from the die region towards the outlet of the die shoulder can be explained by the areas A1–A3 (see Fig. 10a). In area A1, the blankholder force is carried over a large area within the die region, resulting in low nominal contact pressures and subsequently higher friction coefficients compared to values found within the die shoulder ($\mu \approx 0.17$). This observation can be directly correlated to the calculated friction coefficients in Fig. 9a. In area A2, the nominal contact pressure increases towards the die shoulder, decreases at the middle and increases again towards the outlet. This region is characterized by sliding under high nominal contact pressures and surface strains due to bending and unbending of the blank. The relatively high nominal contact pressures yield friction coefficients around $\mu \approx 0.11$. Somewhat higher friction coefficients are found at the middle of the die shoulder ($\mu \approx 0.12$) due to a decrease in nominal contact pressures. In A3, the reduction in nominal contact pressures near the edge of the blank is caused by anticlastic bending, resulting higher friction coefficients ($\mu \approx 0.13$).

The experimentally and numerically obtained punch force–displacement diagrams are compared in Fig. 10b and c. Experiments have been conducted using a punch velocity of 20 mm/s,

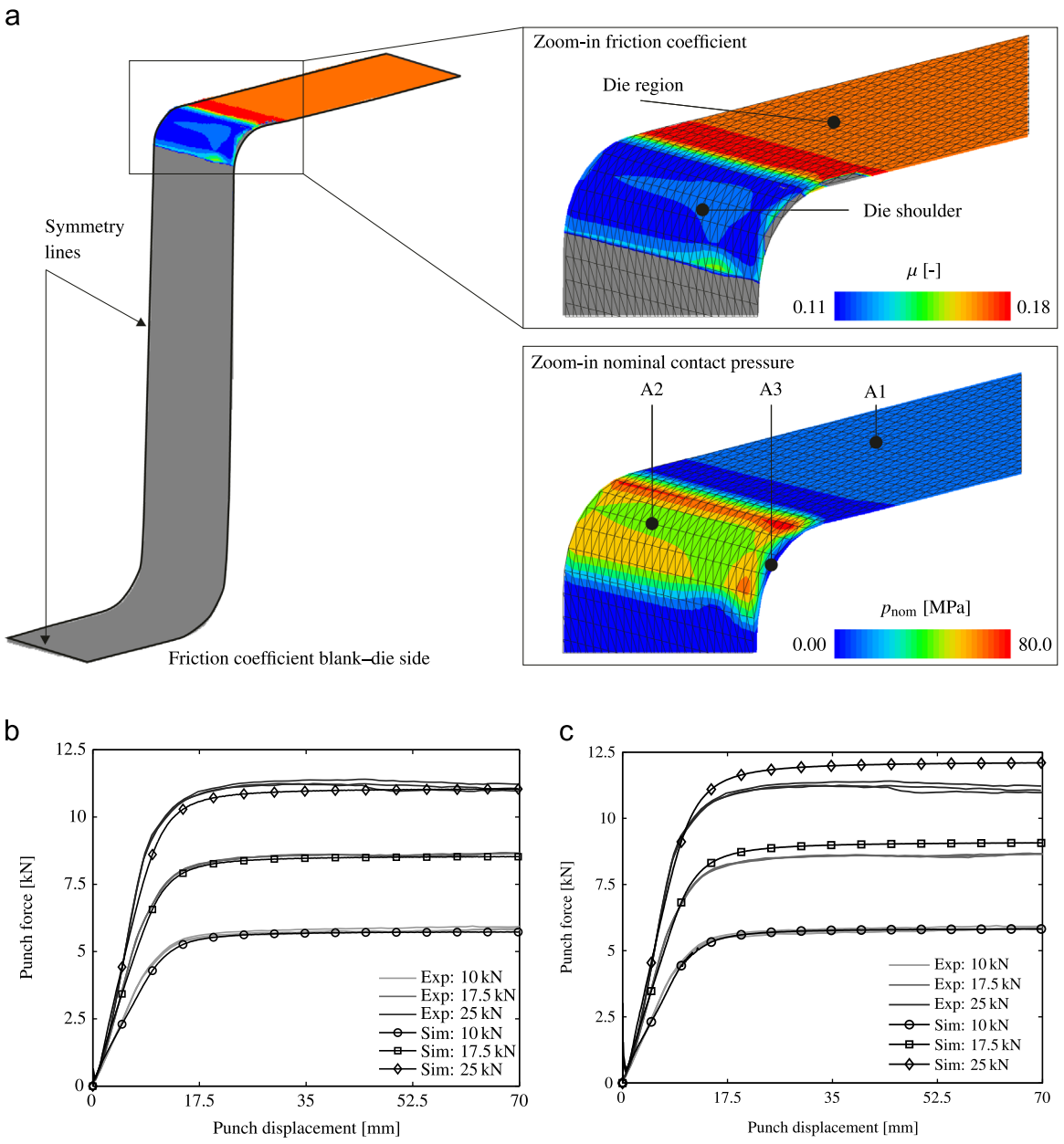

Fig. 10. Impression of numerically obtained friction coefficients top-hat section at 55 mm punch displacement (a) and experimentally/numerically obtained punch force–displacement diagrams for different blankholder forces (b–c) for 0.6 g/m^2 of lubricant (v_{punch} = 20 mm/s and F_{bhf} = 25 kN).

lubricated with Quaker N6130. A lubrication amount of 0.6 g/m^2 was applied to the sheet surfaces before executing the experiments. Fig. 10b shows that the punch force evolves to a steady-state value for all experiments. The small variation in punch forces between triplicates demonstrates the good repeatability of the experiments. As can be seen, the trend of the experimental punch force–displacement diagrams can be predicted precisely by using the proposed boundary lubrication friction model. The simulation time increases by less than 3% compared to using a Coulomb friction model.

Fig. 10c shows a comparison between the experimental results and the FE results using the classical Coulomb friction law. The value of the (constant) friction coefficient is generally unknown in advance and is often adapted based on a trial-and-error approach to mimic experimentally obtained punch forces. The same fitting philosophy is used here, where the Coulomb friction coefficient is obtained by minimizing the error between model and experimental punch forces using a blankholder force of 10 kN. The resulting friction coefficient is $\mu = 0.155$. However, when the blankholder force is increased, the FE results and experimental results start to deviate when using this value for μ. In other words, to describe the punch force–displacement curve, the friction coefficient has to be refitted for each used blankholder force. However, a good agreement for all three blankholder forces is obtained using the advanced friction model.

5.2. Cross-die product

The cross-die product is a product designed by Renault [49], see Fig. 8b. The cross-die product mimics process conditions of automotive parts, introducing complex stress–strain paths in the material and changing contact conditions during forming.

The cross-die tooling consists of a cross-shaped punch, blankholder and die, see Fig. 11a. The dimensions of the blank are 260 × 260 mm having a thickness of 0.8 mm. The punch stroke

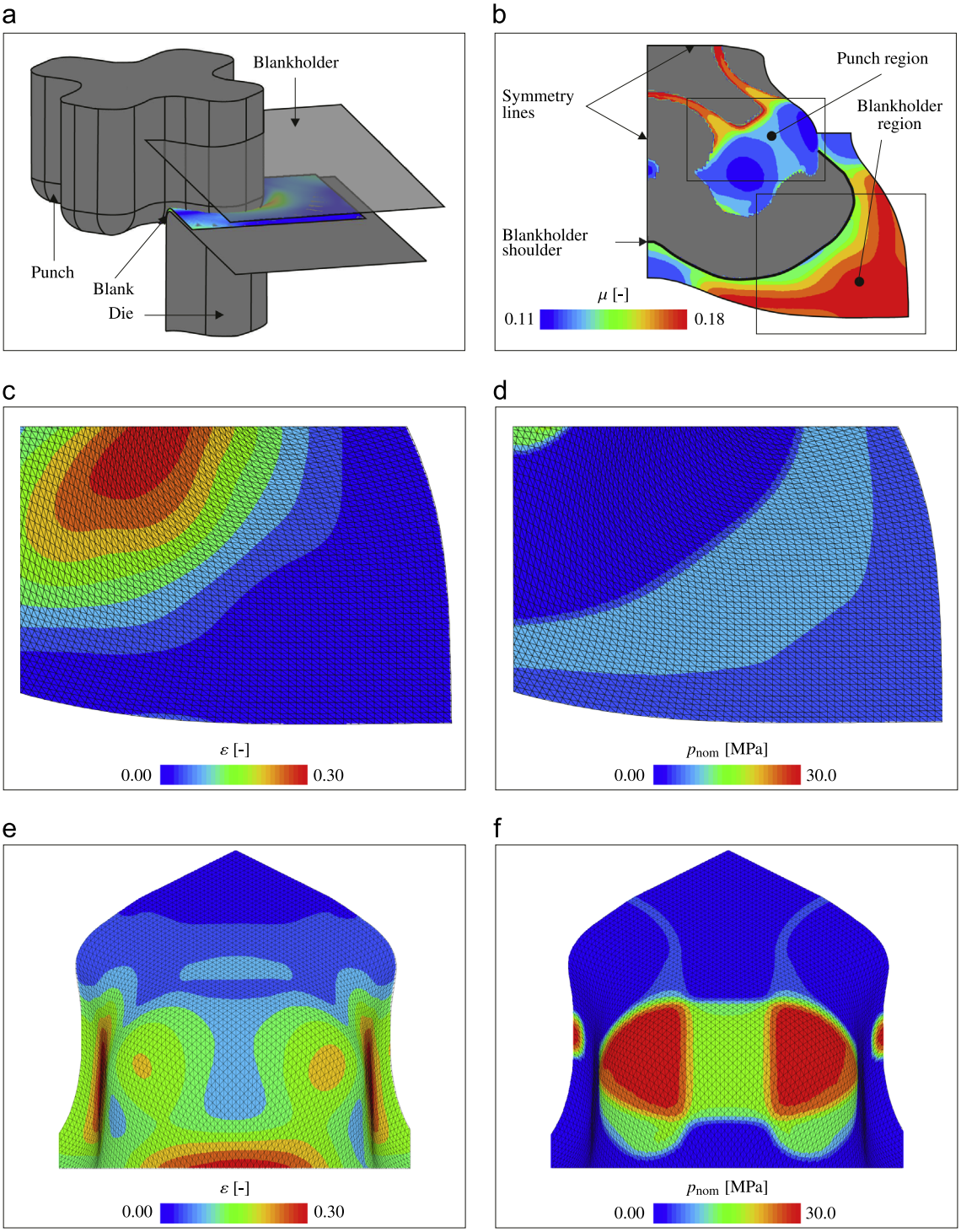

Fig. 11. Schematic view and distribution of friction coefficients (a–b), zoom-in on local process conditions in the blankholder region (c–d) and zoom-in on local process conditions in the punch region (e–f) (punch displacement $=60$ mm, lubricant amount $=0.6$ g/m^2, $v_{punch}=25$ mm/s and $F_{bhf}=150$ kN).

has been set to 60 mm. Process settings of the cross-die experiment are listed in Table 3.

Fig. 11b shows the distribution of friction coefficients at 60 mm punch displacement. Results are shown for the side of the blank in contact with the punch. Friction conditions are influenced by the strains within the sheet material and nominal contact pressures between the tooling and the blank. The distribution of strains and nominal contact pressures are shown in Fig. 11c and d for the punch region and in Fig. 11e and f for the blankholder region. In the blankholder region, relatively low strains and pressures are found. This results in a near constant distribution of friction coefficients around $\mu \approx 0.18$, see Fig. 11b. The strain within the blank increases significantly towards the blankholder shoulder, yielding a decrease in friction coefficients in this region towards $\mu \approx 0.14$. A significant variation in strains and nominal contact pressures can be observed in the punch region, see Fig. 11e and f. The highest strains and nominal contact pressures are found at the punch corners, where friction coefficients decrease towards $\mu \approx 0.11$.

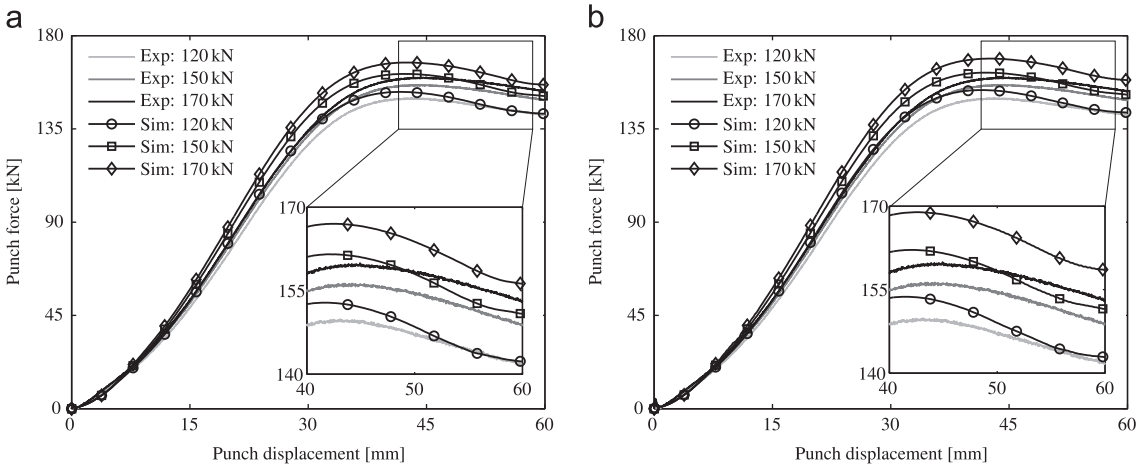

Fig. 12. Punch force–displacement diagrams different blankholder forces, lubrication amount $=0.6\ \mathrm{g/m^2}$ and $v_{\mathrm{punch}} = 25\ \mathrm{mm/s}$. (a) Results obtained by using the advanced friction model. (b) Results obtained by using the Coulomb friction model.

Away from the punch corners, lower strains and nominal contact pressures are observed, consequently leading to higher friction coefficients.

Fig. 12 shows numerically and experimentally obtained punch force–displacement diagrams for different blankholder forces. It is observed that the trend in the development of punch forces is in good agreement with the experimental results (see Fig. 12a). Punch forces are slightly overestimated for punch displacements between 10 mm and 60 mm. The overestimation can be caused by the boundary lubrication friction model, but also by the material model used during the forming simulation. That is, in the cross-die sample the material is much more kinematically constrained than in the top-hat section, reducing the relative influence of friction on punch forces. Although an overestimation in punch forces is predicted for all blankholder forces, overall trends are predicted correctly. The simulation time increases by less than 2% compared to using a Coulomb friction model.

Fig. 12b shows a comparison between numerical and experimental punch forces when using the Coulomb friction model. A constant friction coefficient of $\mu = 0.16$ was used. This value has been obtained from fitting the numerical punch force results to the experimental punch force results when a blankholder force of 120 kN was used. The overall trend is predicted correctly, and corresponds to the trend found when using the boundary lubrication friction model. However, as for the top-hat section, increasing the blankholder force increases the gap between experimental and numerical punch forces.

6. Conclusions

A physically based multi-scale friction model has been developed to describe friction in the boundary lubrication regime. As an input, the model requires 3D tool and workpiece surfaces and specific model parameters. Both the change in surface topography due to loading, sliding and straining actions, and the evolution of friction due to ploughing and adhesion effects is taken care of. An efficient coupling with FE forming simulations has been made by generating friction matrices for a predefined range of nominal contact pressures and strains.

Two deep-drawing applications have been discussed. During forming, local friction coefficients depend on location and time, and rely on external process settings like the blankholder force. An excellent prediction of the punch force is made for a simple-shaped metal product using the advanced friction model. For complex-shaped products the same frictional trends are found as for simple-shaped products. However, the description of the material behavior itself becomes increasingly important, reducing the relative influence of friction.

Numerical results obtained by the boundary lubrication friction model have been compared with results obtained by using the Coulomb friction model. A fitted constant friction coefficient has been used for the Coulomb model. This value only holds for a specific forming process, and depends on the process settings used, like the blankholder force. In order to make an accurate prediction of punch forces, the Coulomb friction coefficient must be adapted for each specific process setting. Contrary to the Coulomb friction model, the advanced friction model does not require any adaptions to the original input data when process settings are changed. Input data is obtained by the calibration presented in this paper and used as such in the FE forming simulations. This clearly demonstrates the increased predictive capabilities of the FE simulation when using the boundary lubrication friction model.

Acknowledgments

This research was carried out under the project number MC1.07289 in the framework of the Research Program of the Materials innovation institute M2i (www.m2i.nl) in cooperation with Tata Steel R&D and the University of Twente. The authors would like to acknowledge R. Boterman, M. Appelman and A. Lourens from Tata Steel for their assistance and support during this study.

Appendix A

The deterministic parameters ω, ξ, β and ψ in Eq. (13) are described by stochastic parameters to make an efficient translation from micro to macro contact modeling. The normalized surface height distribution $\phi_{\mathrm{w}}(z)$ has been introduced for this purpose (see Fig. 1). In the limit of an infinite number of bars, the following expressions hold:

$$F_{\mathrm{N}} = BA_{\mathrm{nom}} \int_{d_{\mathrm{L}}-U}^{\infty} \sigma_{\mathrm{y}}(z)\phi_{\mathrm{w}}(z)\,\mathrm{d}z$$

$$\Delta A \sum_{i=1}^{N} \Delta z_i = A_{\mathrm{nom}} \int_{d_{\mathrm{L}}}^{\infty} (z-d_{\mathrm{L}})\phi_{\mathrm{w}}(z)\,\mathrm{d}z$$

$$\Delta A \sum_{j=1}^{N^*} \Delta z_j = A_{\mathrm{nom}} \int_{d_{\mathrm{L}}-U_{\mathrm{L}}}^{d_{\mathrm{L}}} (z-d_{\mathrm{L}}+U_{\mathrm{L}})\phi_{\mathrm{w}}(z)\,\mathrm{d}z$$

$$\Delta A \sum_{j=1}^{N^*} \Delta u_j = A_{\text{nom}} \int_{d_L - U_L}^{d_L} (d_L - z)\phi_w(z)\,dz$$
$$\Delta A \sum_{l=1}^{N^{**}} \Delta u_l = A_{\text{nom}} \int_{-\infty}^{d_L - U_L} U_L \phi_w(z)\,dz$$
$$n_s w \sum_{k=1}^{N+N^*} \Delta s_k = L_s \int_{d_L - U_L}^{\infty} (z - d_L + U_L)\phi_w(z)\,dz \quad (A.1)$$

with $A_{\text{nom}} = M\Delta A$ and $L_s = M n_s w$.

The energy factors, in deterministic and stochastic form, can now be written as

$$\omega = \frac{\sum_{k=1}^{N+N^*} F_{N,k}\Delta z_k}{F_N} = \frac{\int_{d_L}^{\infty} \sigma_y(z)(z-d_L)\phi_w(z)\,dz + \int_{d_L-U_L}^{d_L} \sigma_y(z)(z-d_L+U_L)\phi_w(z)\,dz}{\int_{d_L-U_L}^{\infty} \sigma_y(z)\phi_w(z)\,dz} \quad (A.2)$$

$$\xi = \Delta A \sum_{k=1}^{N+N^*} \sigma_{y,k}\Delta z_k = A_{\text{nom}} \left(\int_{d_L}^{\infty} \sigma_y(z)(z-d_L)\phi_w(z)\,dz + \int_{d_L-U_L}^{d_L} \sigma_y(z)(z-d_L+U_L)\phi_w(z)dz \right) \quad (A.3)$$

$$\beta = \Delta A \left(\sum_{j=1}^{N^*} \sigma_{y,j}\Delta u_j + \sum_{l=1}^{N^{**}} \sigma_{y,l}\Delta u_l \right) = A_{\text{nom}} \left(\int_{d_L-U_L}^{d_L} \sigma_y(z)(d_L - z)\phi_w(z)\,dz + \int_{-\infty}^{d_L-U_L} \sigma_y(z) U_L \phi_w(z)\,dz \right) \quad (A.4)$$

and

$$\psi = \left(1 - \frac{A_{\text{real}}}{A_{\text{nom}}}\right) n_s w \sum_{k=1}^{N+N^*} \sigma_{y,k}\Delta s_k^2 = L_s \int_{-\infty}^{d_L-U_L} \phi_w(z)\,dz \left(\int_{d_L-U_L}^{\infty} \sigma_y(z)(z-d_L+U_L)^2 \phi_w(z)\,dz \right) \quad (A.5)$$

where the following relation has been used:

$$1 - \frac{A_{\text{real}}}{A_{\text{nom}}} = 1 - \alpha_L = 1 - \int_{d_L-U_L}^{\infty} \phi_w(z)\,dz = \int_{-\infty}^{d_L-U_L} \phi_w(z)\,dz \quad (A.6)$$

In which the fractional real contact area α_L has been introduced.

References

[1] Wanheim T, Bay N. Model for friction in metal forming processes. Gen Assem CIRP 1978;27:189–94.
[2] Grüebler R. Simulation des umformtechnischen Tribosystems [Ph.D. thesis]. ETH-Zurich; 2002.
[3] Ludwig M, Müller C, Groche P. Simulation of dynamic lubricant effects in sheet metal forming processes. Key Eng Mat 2010;438:171–8.
[4] Hol J, Alfaro MVC, de Rooij MB, Meinders T. Advanced friction modeling for sheet metal forming. Wear 2011;286–287:66–78.
[5] Shih HC, Wilson WRD. Effects of contact pressure and strain on friction in sheet-metal forming. Tribol Trans 1999;42:144–51.
[6] Lo SW, Yang TC, Shih ZM. Effects of surface roughening on asperity flattening. Tribol Lett 2009;35:67–75.
[7] Greenwood JA, Williamson JBP. Contact of nominally flat surfaces. Proc R Soc Lond Ser A, Math Phys Sci 1966;295:300–19.
[8] Westeneng, JD. Modelling of contact and friction in deep drawing processes [Ph.D. thesis]. University of Twente; 2001.
[9] Zhao DMMY, Chang L. An asperity microcontact model incorporating the transition from elastic deformation to fully plastic flow. J Tribol 2000;122:86–93.
[10] Pullen J, Williamson JBP. On the plastic contact of rough surfaces. Proc R Soc Lond Ser A, Math Phys Sci 1972;327:159–73.
[11] Zhao Y, Chang L. A model of asperity interactions in elastic-plastic contact of rough surfaces. J Tribol 2001;123:857–64.
[12] Wilson WRD, Sheu S. Real area of contact and boundary friction in metal forming. Int J Mech Sci 1988;30:475–89.
[13] Sutcliffe MPF. Surface asperity deformation in metal forming processes. Int J Mech Sci 1988;30:847–68.
[14] Tian X, Bhushan B. A numerical three-dimensional model for the contact of rough surfaces by variational principle. J Tribol 1996;118:33–42.
[15] Korzekwa DA, Dawson PR, Wilson WRD. Surface asperity deformation during sheet forming. Int J Mech Sci 1992;34(7):521–39.
[16] Tabor D. Junction growth in metallic friction: the role of combined stresses and surface contamination. Proc R Soc Lond 1959;251:378–93.
[17] McFarlane JS, Tabor D. Relation between friction and adhesion. Proc R Soc Lond Ser A 1950;251:244–53.
[18] Parker R, Hatch D. The static coefficient of friction and the area of contact. Proc Phys Soc Sect B 1950;63:185–97.
[19] Kayaba T, Kato K. Experimental analysis of junction growth with a junction model. Wear 1978;51:105–16.
[20] Ovcharenko A, Halperin G, Etsion I. In situ and real-time optical investigation of junction growth in spherical elastic-plastic contact. Wear 2008;264:1043–50.
[21] Emmens WC. Tribology of flat contacts and its application in deep drawing [Ph.D. thesis]. University of Twente; 1997.
[22] Lo SW, Tsai SD. Real-time observation of the evolution of contact area under boundary lubrication in sliding contact. J Tribol 2002;124:229–38.
[23] Wilson WRD. Friction models for metal forming in the boundary lubrication regime. Am Soc Mech Eng 1988;10:13–23.
[24] Challen JM, Oxley PLB. An explanation of the different regimes of friction and wear using asperity deformation models. Wear 1979;53:229–43.
[25] Challen JM, Oxley PLB. Slip-line fields for explaining the mechanics of polishing and related processes. Int J Mech Sci 1984;26:403–18.
[26] Nayak PR. Random process model of rough surfaces in plastic contact. Wear 1973;26:305–33.
[27] Greenwood JA. A note on Nayak's third paper. Wear 2007;262:225–7.
[28] Poon CY, Bhushan B. Comparison of surface roughness measurements by stylus profiler, AFM and non-contact optical profiler. Wear 1995;190:76–88.
[29] Ma X, de Rooij M, Schipper DJ. A load dependent friction model for fully plastic contact conditions. Wear 2012;269:790–6.
[30] Bergström Y. A dislocation model for the stress-strain behaviour of polycrystalline α-Fe with special emphasis on the variation of the densities of mobile and immobile dislocations. Mater Sci Eng 1970;5:193–200.
[31] van Liempt P. Workhardening and substructural geometry of metals. J Mater Process Technol 1994;45:459–64.
[32] Vegter H, van den Boogaard AH. A plane stress yield function for anisotropic sheet material by interpolation of biaxial stress states. Int J Plast 2006;22:557–80.
[33] Vegter H. On the plastic behaviour of steel during sheet forming [Ph.D. thesis]. University of Twente; 1991.
[34] Saha PK, Wilson WRD. Influence of plastic strain on friction in sheet metal forming. Wear 1994;172:167–73.
[35] Hokkirigawa K, Kato K. An experimental and theoretical investigation of ploughing, cutting and wedge formation during abrasive wear. Tribol Int 1988;21:51–7.
[36] Hol J. Multi-scale friction modeling for sheet metal forming [Ph.D. thesis]. University of Twente; 2013.
[37] Hu MK. Visual pattern recognition by moment invariants. IRE Trans Inf Theory 1962:179–87.
[38] Lim JS. Two-dimensional signal and image processing. Prentice Hall; 1990.
[39] de Boor C. On calculating with B-splines. J Approx Theory 1972;6:50–62.
[40] Toose E. Private communication; 2010.
[41] de Rooij M. Tribological aspects of unlubricated deepdrawing processes [Ph.D. thesis]. University of Twente; 1998.
[42] Grüebler R, Hora P. Temperature dependent friction modeling for sheet metal forming. Int J Mater Form 2009;2:251–4.
[43] Krauer J, Hora P. Enhanced material models for the process design of the temperature dependent forming behavior of metastable steels. Int J Mater Form 2012;5:361–70.
[44] Courtney-Pratt JS, Eisner E. The effect of a tangential force on the contact of metallic bodies. Proc R Soc Lond Ser A, Math Phys Sci 1957;238:529–50.
[45] Schedin E. Micro-mechanisms of sheet-tool contact in sheet metal forming [Ph.D. thesis]. Royal Institute of Technology Sweden; 1991.
[46] Roll K, Wiegand K, Hora P. Benchmark 2—influence on drawbeads on the springback behaviour—Part A: Physical tryout report. In: Proceedings of Numisheet 2008—seventh international conference on numerical simulation of 3D sheet metal forming processes—Part B; 2008. p. 45–52.
[47] Filzek F, Ludweg M, Groche P. Improved FEM simulation of sheet metal forming with friction modelling using laboratory tests. In: Fifteenth international deep drawing research group conference, IDDRG2011; 2011.
[48] van den Boogaard AH, Huétink J. Simulation of aluminium sheet forming at elevated temperatures. Comput Methods Appl Mech Eng 2006;195:6691–709.
[49] Maeder G. Advanced methods in material forming. Berlin, Heidelberg: Springer; 2007, p. 19–33.